PAPER

Check for updates

Comparison of nano-structured transition metal modified tri-metal MgMAl–LDHs (M = Fe, Zn, Cu, Ni, Co) prepared using co-precipitation†

Bianca R. Gevers, [ID] *[a] Sajid Naseem, [ID] [b] Andreas Leuteritz[b] and Frederick J. W. J. Labuschagné[a]

Comparison of layered double hydroxides (LDHs) synthesised using different methods, conditions and post-treatment is difficult to achieve because these greatly modify their material properties. This paper aims to provide a comparison of material properties for modified quintinite, where all LDHs were synthesised at the same conditions – thus allowing for direct comparison of the material properties obtained. Nano-structured materials were formed in all cases. The nano-structured transition metal (TM) MgMAl–LDHs were synthesised using constant pH co-precipitation. Five TMs (M = Fe, Co, Ni, Cu, Zn) were included in the LDH layers with molar substitutions of 0.5%, 1%, 5%, 10%, and 25% based on Mg-replacement for divalent TM cations and Al-replacement for trivalent TM cations. The materials were characterised using powder X-ray diffraction (XRD), X-ray fluorescence spectroscopy (XRF), scanning electron microscopy (SEM), attenuated total reflectance Fourier transform infrared analysis (ATR-FTIR), thermogravimetric analysis (TGA) and particle size analysis (PSA). The modified LDHs were synthesised free of major by-products and with similar morphologies. It could be shown that the crystallite dimensions varied between the different TM substitutions, that morphological changes were visible for some of the TMs used, that the processability depended on the TMs substituted, and that the substitution of TMs influenced the thermal stability of the LDHs.

1 Introduction

LDHs are anionic clays with the general formula

$$[M^{II}_{1-x}M^{III}_x(OH)_2][X^{q-}_{x/q} \cdot nH_2O]$$

where $[M^{II}_{1-x}M^{III}_x(OH)_2]$ describes the composition of the LDH layers consisting of trivalent (M^{III}) and divalent (M^{II}) metal cations, while $[X^{q-}_{x/q} \cdot nH_2O]$ represents the composition of the anionic interlayer. Further, x is the molar fraction of trivalent cations to total metal cations in the layer structure and is typically limited to $0.1 \leq x \leq 0.33$. X represents the interlayer anion with charge q.[1] LDHs have received increasing research attention due to their simple adaptability and tailoring options with respect to metal composition, anion usage and morphology.[1,2]

LDHs are most frequently synthesised using co-precipitation due to the ease of preparation for most compositions and the purity of the LDHs formed. Other options include urea hydrolysis, sol–gel synthesis and hydrothermal synthesis.[1,3]

One of the most common LDHs is hydrotalcite, which naturally occurs as $Mg_6Al_2(OH)_{16}CO_3 \cdot 4H_2O$ and can, with carbonate anions in the interlayer space, be synthetically produced with ratios of divalent to trivalent metal cations of 1.0–3.0.[1] Hydrotalcite can be modified to include other metals in its layer structure and is thus frequently investigated as a support structure for TMs. A variety of such substitutions have been performed in literature. In fact, publications exist with many different combinations of metals in the layer, and almost all metals have successfully been included in LDHs' layers.[4]

A subdivision of the hydrotalcite supergroup comprises the quintinite-group which consists of LDHs where the ratio M^{II+}/M^{II+} is 2 : 1 and typical anions (CO_3^{2-} and Cl^-) and water are present in the interlayer.[5] Quintinite has the chemical formula $Mg_4Al_2(OH)_{12}CO_3 \cdot 3H_2O$. The use of modified quintinite is widespread (albeit the LDHs are typically named hydrotalcite-like materials).

As mentioned by Mills *et al.* (2012), the predominant mentions of divalent metals in the layers of LDHs within the hydrotalcite supergroup are Mg, Ca, Mn, Fe, Ni, Cu and Zn, while the predominant trivalent metals are Al, Mn, Fe, Co and Ni.[5] Common interlayer anions include CO_3^{2-}, Cl^-, SO_4^{2-}, OH^-, S^{2-} and $[Sb(OH)_6]^-$, the most common one being CO_3^{2-}.[5] For

[a]University of Pretoria, Lynnwood Road, 0002, Pretoria, South Africa. E-mail: bianca. gevers@tuks.co.za

[b]Leibniz-Institut für Polymerforschung Dresden e. V., Hohe Straße 6, 01069, Dresden, Germany

this study, the divalent metals Co, Ni, Cu and Zn, and trivalent metal Fe were chosen to modify the layer composition of standard quintinite. All LDHs were prepared with CO_3^{2-} in the interlayer, as this was found to be the most common anion used in modified quintinite. The TMs for substitution were chosen for their variety of applications across catalysis, renewable energy generation, environmental remediation, drug delivery and polymer stabilisation – all big or upcoming fields of application for LDHs.[1,6–8]

Some examples of quintinite modification within these fields include: catalysis (ethylbenzene dehydrogenation,[9] hydrocarbon oxidation,[10] CO_2 reforming of methane,[11] dry reforming of methane[12]), drug delivery (NSAID release[13]), renewable energy (H_2 generation,[14] transesterification of soybean oil[15]), environmental remediation (fluoride absorption,[16] wet air oxidation of Basic Yellow 11,[17] N_2O decomposition,[18] methyl orange adsorption[19]) and polymer stabilisation/functional additives (PVC stabilisation,[20] HCl scavenging in PVC,[21] UV degradation stabiliser[22]).

Some researchers have performed investigations into the influence of the type and amount of TM substituted into LDH layers. A comprehensive search was conducted to find literature relevant to the synthesis and characterisation of modified quintinite. The results of the search are listed in Table 1.

As clearly visible from the table, papers that focus on the synthesis and characterisation of TM-modified quintinite and compare a variety of TMs are quite rare. Of the papers listed in Table 1, Rivera et al. (2006), Pavel et al. (2012) and Tsyganok et al. (2006) provided a comparison between different substituted TMs at the same substitution percentage.[27,29,33]

Some authors have investigated the effect of different amounts of TMs substituted into quintinite layers. Examples of these are the varying substitution of Fe,[14,16,17] Co,[30,31] Ni,[15,17,18] and Zn,[19,20,22] into quintinite. However, no papers (other than our previous paper on the urea hydrolysis synthesis of TM-modified LDHs,[28] comparing the effects of two substitutions) could be found that focused on the synthesis, characterisation and comparison of varying amounts and types of TM substituted into quintinite specifically and using co-precipitation. This could be a result of the thermodynamic stability of the LDH phase depending on the synthesis pH, thus favouring the precipitation of divalent metal hydroxides if an unsuitable synthesis pH was chosen and producing impure LDH phases difficult to compare. Based on the solubility products of di-metal quintinite ($[M_4Al_2(OH)_{12}]CO_3 \cdot nH_2O$), the formation of divalent hydroxides is favoured above pH ≈ 10 for M = Zn, pH ≈ 9 for M = Co, pH ≈ 8 for M = Ni and pH ≈ 12 for M = Mg.[3]

What is also evident from Table 1, is that the synthesis conditions and methods varied in most studies. As the product LDH phases' morphology and physical characteristics are heavily influenced by the synthesis method and conditions used, it renders the research that has already been performed difficult if not impossible to compare. Because of the difficulty of comparison between the different data sets, this paper aims to give the reader information on the effect of the amount and type of TM-substituted into the LDH layers with focus on purity,

structural differences, morphological differences and thermal stability differences for LDHs all synthesised at the same conditions.
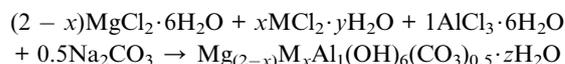
2 Experimental

2.1 Materials

Chemically pure (CP), reagent grade (RG) or analytical grade (AR) reactants were used for all experiments. $AlCl_3 \cdot 6H_2O$ (CP), $MgCl_2 \cdot 6H_2O$ (CP), $ZnCl_2$ (CP), $FeCl_3 \cdot 6H_2O$ (CP), $CoCl_2 \cdot 6H_2O$ (AR), NaOH (AR) and Na_2CO_3 (AR) were sourced from ACE Chemicals. $NiCl_2 \cdot 6H_2O$ (AR) and $CuCl_2 \cdot 2H_2O$ (AR) were obtained from Merck, and $FeCl_3$ (RG) from Sigma Aldrich. Deionised water was used for all experiments.
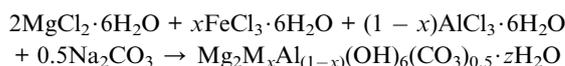
2.2 Material preparation

All LDHs were synthesised by making use of the constant pH co-precipitation method. The stoichiometric amounts of metal salts were dissolved in deionised water to form a 2.5 M solution (based on cations). Na_2CO_3 was used in excess to ensure availability of carbonate anions in solution. The salt solution was added into a 0.4 M Na_2CO_3 solution in a dropwise fashion while maintaining a pH of 11 ± 0.3 in all experiments by adding 10 M NaOH solution as required. The synthesis pH was specifically chosen to be higher than the optimum/frequently chosen synthesis pH for hydrotalcite synthesis (pH = 10)[38] so that all metal species are kept well above their theoretical hydroxide formation limit.[3,39] Further, the precipitation was carried out at high supersaturation to limit the formation of the hydroxides. The resulting slurry was stirred vigorously at 500 rpm throughout the reaction. The precipitated LDH was filtered off using vacuum filtration, washed with 5 L of deionised water, and dried at 60 °C overnight (18 h).

MgAl–LDHs with five TM substitutions (Fe, Co, Ni, Cu and Zn) were prepared with substitution percentages (s) of 0.5%, 1%, 5%, 10% and 25%. Hereby, Mg was substituted with the divalent metal cations of Co, Ni, Cu, and Zn and Al was substituted with trivalent Fe cations. The stoichiometrically correct amounts of salts for the divalent metal (Co, Ni, Cu and Zn) substituted LDHs were calculated using

$$(2 - x)MgCl_2 \cdot 6H_2O + xMCl_2 \cdot yH_2O + 1AlCl_3 \cdot 6H_2O + 0.5Na_2CO_3 \rightarrow Mg_{(2-x)}M_xAl_1(OH)_6(CO_3)_{0.5} \cdot zH_2O$$

The stoichiometrically correct amounts of salts for the trivalent metal (Fe) substituted LDHs were calculated using

$$2MgCl_2 \cdot 6H_2O + xFeCl_3 \cdot 6H_2O + (1 - x)AlCl_3 \cdot 6H_2O + 0.5Na_2CO_3 \rightarrow Mg_2M_xAl_{(1-x)}(OH)_6(CO_3)_{0.5} \cdot zH_2O$$

In both of these equations, x was calculated by multiplying s with the number of moles of Mg or Al theoretically required. The samples were named accordingly, using the general formula MgMAl-s. Here, M indicates the substituted TM and s the molar substitution percentage.

Table 1 Summary of literature available on the topic of synthesis and characterisation of LDHs modified with TMs Fe, Co, Ni, Cu and Zn[a]

Anion	Mg : Al ratio	Subs.	Syn. pH	SynM	Ref.
MgFeAl–LDH					
CO_3^{2-}	5.66, 2.33, 1 & 0.43 : 1	33.33, 16.66, 10, 7	9.6–9.9	hls CP	23,24
CO_3^{2-}	3 : 2	25, 50, 75	9	CP	25
C + S	2 : 1	50	2.4–13	v CP	26
CO_3^{2-}	2 : 1	4, 8, 12, 16, 20, 40, 60, 80	9.5	CP	14
CO_3^{2-}	2 : 1	16.66, 33.33, 50, 66.66, 83.33	—	sa CP	16
NO_3^-	3 : 1	5	10	CP	27
CO_3^{2-}	2 : 1	5, 10	—	UH	28
MgCoAl–LDH					
CO_3^{2-}	3.5 : 1	12.5	10	CP	29
CO_3^{2-}	2 : 1	3, 5	—	UH	30
$C_8H_4O_4$	2.33, 1 : 1	20, 40, 60, 80	6.5	CP	31
CO_3^{2-}	9, 10 : 1	11.11, 20	9	CP	32
NO_3^-	3 : 1	5	10	CP	27
CO_3^{2-}	2 : 1	5, 10	—	UH	28
MgNiAl–LDH					
CO_3^{2-}	3.5 : 1	12.5	10	CP	29
NO_3^-	3 : 1	5	10	CP	27
NO_3^-	2, 3, 4 : 1	50	13	m CP	33
CO_3^{2-}	7, 3 : 1	33.33, 66.67, 85.7	10	CP	34
CO_3^{2-}	5, 3, 1, 0.33, 0.2 : 1	8	10.5	CP	35
CO_3^{2-}	2 : 1	5, 10	—	UH	28
MgCuAl–LDH					
CO_3^{2-}	3.5 : 1	12.5	10	CP	29
CO_3^{2-}	1–5 : 1	1, 3, 5, 7, 10, 20	10	CP	36
NO_3^-	3 : 1	5	10	CP	27
CO_3^{2-}	2 : 1	5, 10	—	UH	28
MgZnAl–LDH					
CO_3^{2-}	5.67	25, 50, 75	—	UH	37
NO_3^-	3 : 1	5	10	CP	27
NO_3^-	2, 3, 4 : 1	50	13	m CP	33
CO_3^{2-}	2 : 1	12.5, 50, 80	—	UH	19
CO_3^{2-}	2 : 1	5, 10	—	UH	28

[a] SynM: synthesis method, CP: co-precipitation, hls CP: high and low saturation CP, v CP: variable CP, m CP: microwave CP, UH: urea hydrolysis, sa CP: simultaneous addition CP, C + S: CO_3^{2-} + SO_4^{2-}.

2.3 Materials characterisation

X-ray diffraction measurements were performed on a Panalytical X'Pert PRO X-ray diffractometer in θ–θ configuration, equipped with Fe-filtered Co-Kα radiation (1.789 Å) and an X'Celerator detector and variable-divergence- and fixed receiving slits. Samples were prepared according the standardised Panalytical backloading system, which facilitates the nearly random distribution of the particles. Data were collected in the angular range $5° \leq 2\theta \leq 80°$, with a step size of $0.008° \, 2\theta$ and a 13 s scan step time. The phases were identified using X'Pert HighScore Plus software. The spectra were converted from variable slit to fixed slit prior to phase identification. The detection limit for phases was 2%.

X-ray fluorescence (XRF) analysis was performed using a Thermo Fisher ARL Perform'X Sequential XRF instrument. The samples were dried at 100 °C and roasted at 1000 °C to determine loss on ignition (LOI). 1 g roasted sample (where available, if not, maximum grams remaining after roasting) was then placed together with 6 g of $Li_2B_4O_7$ into a Pt/Au crucible and fused. Analyses were executed using the corresponding Quantas software.

Scanning electron microscopy (SEM) images were taken with a Zeiss Gemini Ultra Plus FEG SEM, and a Zeiss Gemini 2 Crossbeam 540 FEG SEM. The samples were prepared by evenly distributing the samples on carbon tape on an aluminium stub and coating it with two layers of carbon (angles: 0°, −45° and +45°) using a sputter coater. The micrographs were taken at 1 keV.

Thermogravimetric analysis (TGA) was performed with a heating rate of 10 °C min^{-1} using a TGA Q5000 from TA instruments in an inert nitrogen atmosphere.

ATR-FTIR spectra were obtained using a PerkinElmer 100 Spectrophotometer. Samples were pressed in place with a force arm. Spectra were obtained in the range of 550–4000 cm^{-1} each with 32 scans at a resolution of 2 cm^{-1}.

The particle size analysis (PSA) was carried out using a Malvern Mastersizer 3000. Each sample was sieved to remove large agglomerates and diluted with distilled and deionised water. The sample was dispersed using tetrasodium pyrophosphate, blended, filtered and the filter cake re-dispersed in distilled and deionised water by shaking.

3 Results

3.1 Structure, composition and purity

The XRD patterns obtained for the synthesised samples are shown in Fig. 1 and a summary of the data obtained from XRD analysis (angular reflection positions, *d*-spacing, crystal parameters and crystallite sizes) is given in the ESI.† All samples were observed to have very similar patterns and clear (003), (006), (009), (110) and (115) reflections, as expected for an LDH in the rhombohedral $R\bar{3}m$ space group. The observed patterns show the expected reflections for synthetic quintinite in the rhombohedral (3R) stacking sequence prepared at near-ambient conditions.[40] Broad reflections on XRD patterns for LDHs can indicate the formation of small crystallites and stacking faults.[41] From comparison of our data to previous data obtained from samples prepared using urea hydrolysis,[28] it could be concluded that the broad peaks observed in this study are indicative of the formation of small crystallites.[41]

The materials were prepared with great purity. No immediately visible reflections indicating an impurity phase were found for any LDH other than MgCuAl-5. However, three other LDHs were found to contain very small amounts of an additional phase. The impurity phases identified through XRD analysis showed that jamborite ($Ni(OH)_2 \cdot NiOOH$), calumetite ($Cu(OH,Cl)_2 \cdot 2H_2O$) and caresite ($Fe_4Al_2(OH)_{12}(CO_3) \cdot 3H_2O$) were present in very small amounts in MgNiAl-0.5, MgNiAl-5, MgCuAl-5 and MgFeAl-10, respectively. Halo-formation, if present, was found to be small in the samples prepared, thus indicating that the LDHs were mostly synthesised free of appreciable amounts of amorphous material. However, it could not be excluded that some of the LDH phases were formed with low crystallinity, thus closely resembling amorphous material.

Further, the LDHs showed very similar peak definitions and intensities. For all but four LDHs, the intensity of the main reflection was higher compared to that of unmodified MgAl–LDH (Fig. 2). The Fe-, Co- and Zn-substituted LDHs all showed a definite increase in primary reflection intensity (PRI) with an increase in TM substitution. The PRIs of the Ni- and Cu-substituted LDHs varied upon an increase in TM substitution. The PRIs of the Ni-substituted LDHs were found to increase, except for a dip at 10% substitution. The net change in PRI of the Cu-substituted LDHs was positive; a zig-zag upwards trend seemed to exist. It was concluded that the general trend in PRI increase with an increase in TM substitution was significant enough in the Fe, Co, Zn and Cu-substituted LDHs to potentially relate these to increases in crystallinity rather than constructive interference due to preferential platelet orientation upon powder pressing during the XRD sample preparation – a phenomenon commonly observed in the XRD analysis of clays.[42] This could be further substantiated by the increased
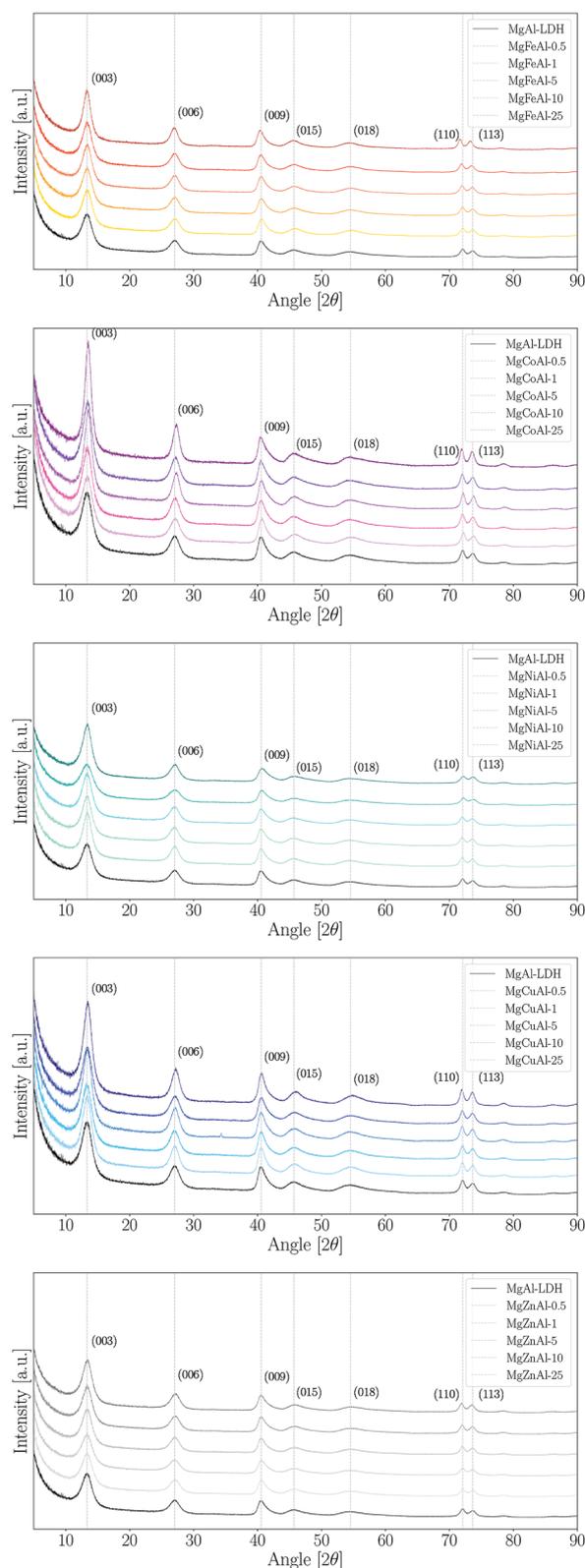

Fig. 1 XRD patterns of the TM-substituted MgMAl–LDHs synthesised.

narrowness of the PRI with an increase in TM substitution. However, because multiple factors influence the reflection intensity and width (*e.g.* crystallite size and crystallinity) no
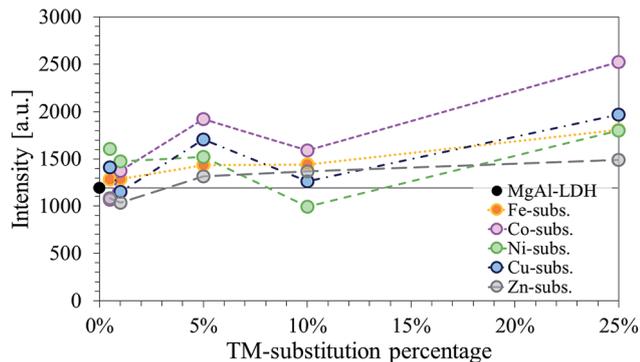
Fig. 2 Comparison of the background adjusted intensities of the primary (003) reflection shown as a function of the TM-substitution percentage used to modify the MgMAl–LDHs with M = Fe, Co, Ni, Cu and Zn.

definite conclusion could be drawn on the increase in the crystallinity of the LDHs with TM substitution.

Considering the XRD patterns shown in Fig. 1, it can be observed that some deviations in the position of the (most significantly) (003) and (110) reflections existed. Crystal parameters c and a were thus calculated in order to quantify structural changes in the LDHs. Changes in the c- and a-parameter with TM substitution are shown in Fig. 3. Bragg's law ($n\lambda = 2d \sin \theta$) was used to calculate the layer spacings d_{001} and d_{110} of the LDH. An average parameter c was calculated as shown by dos Reis *et al.* (2004)[43] and using the relation that $d_{003} = 2d_{006} = 3d_{009}$ for LDHs of rhombohedral symmetry[2] so that $c = 3(1/3(d_{003} + 2d_{006} + 3d_{009})) = d_{003} + 2d_{006} + 3d_{009}$. Parameter a was calculated using $a = 2d_{110}$.[2] It could be shown that the a-parameter increased linearly for the Fe-substituted LDHs and almost linearly with Cu- and Zn-substitution. The most significant increase in a-parameter was observed for the Fe-substituted LDHs. Only small increases in the a-parameter

were observed for Cu- and Zn-substitution. The a-parameter varied for Co-substitution, albeit an increased a-parameter was observed for the 1%, 10% and 25% substituted LDHs. A decline in the a-parameter was observed upon Ni-substitution.

Changes in the a-parameter are a function of changes in the layer structure of LDHs. Being independent of the interlayer composition, the a-parameter can be used to determine successful layer composition modification.[2] Considering the atomic radii of the VI coordinated cations in the crystal lattice (Mg^{2+} = 0.72 Å, Co^{2+} = 0.745 Å, Ni^{2+} = 0.69 Å, Cu^{2+} = 0.73 Å, Zn^{2+} = 0.74 Å, Al^{3+} = 0.535 Å and Fe^{3+} = 0.645 Å)[44] the results correspond very well to the expected results for the modification of the LDH layer composition. We believe that the fluctuations in a-parameter observed for the Co-substituted samples occurred due to a change in valence state of the Co^{2+} cation to Co^{3+} ($r(Co^{3+}$ = 0.545 − 0.61 Å)).

The results of the c-parameter calculations showed that some deviation existed in the layer distance between all groups of TM-substituted LDHs and between the different substitution percentages. Changes in the c-parameter are a function of the cation radius of the metals in the layer, as well as the number of water molecules and orientation of the anions (including coordination of the water and anions) within the interlayer.[2] The differences seen here were found to match the change in interlayer water present in the LDHs (see TGA discussion) taking into account the layer thickness (a-parameter).

XRF analysis was used to ascertain the layer composition of the LDHs formed. Table 2 shows that the M^{2+}/M^{3+} ratio was close to 2 : 1 for all synthesised LDHs. The desired TM substitution was closely matched for all but the Co-substituted LDHs.

XRF analysis revealed that other impurity cations were present in the samples, stemming from impurities in the chemicals used for synthesis. The Ni-, Zn- and Co-substituted samples contained impurities of Si and Ca, the Fe-substituted samples impurities of Si, Ca and S, and the Cu-substituted
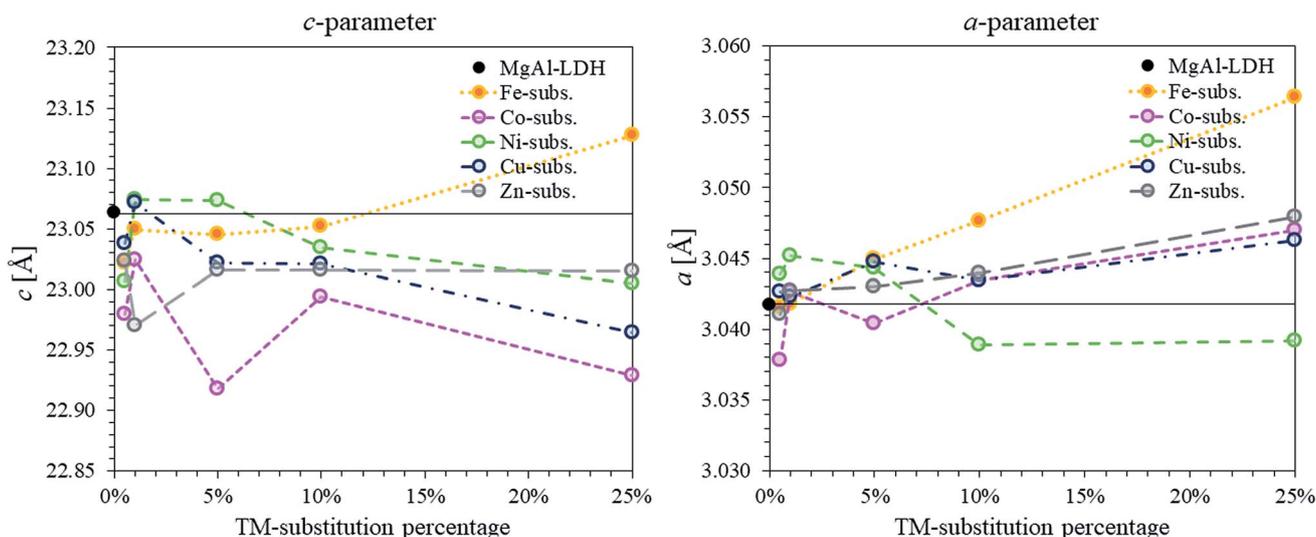

Fig. 3 Comparison of c- and a-parameters calculated for the series of TM-substituted MgMAl–LDHs with M = Fe, Co, Ni, Cu and Zn. The parameters were calculated from the XRD data shown in Fig. 1.

Table 2 Results of the molar amounts of MgO, Al_2O_3 and TM-oxide found in the samples in conjunction with the calculated molar M^{II}/M^{III} ratios and the achieved substitution percentage

Name	MgO	Al_2O_3	TM-oxide	Ratio	Subs.
MgAl	0.811	0.192	0.000	2.11	0
MgNiAl-0.5	0.831	0.186	0.005	2.24	0.58%
MgNiAl-1	0.846	0.176	0.007	2.43	0.80%
MgNiAl-5	0.772	0.180	0.045	2.26	5.51%
MgNiAl-10	0.682	0.182	0.086	2.11	11.22%
MgNiAl-25	0.581	0.162	0.193	2.39	24.93%
MgCuAl-0.5	0.814	0.182	0.004	2.24	0.53%
MgCuAl-1	0.799	0.189	0.009	2.13	1.13%
MgCuAl-5	0.779	0.184	0.043	2.23	5.24%
MgCuAl-10	0.712	0.180	0.081	2.20	10.24%
MgCuAl-25	0.546	0.170	0.194	2.18	26.18%
MgFeAl-0.5	0.796	0.189	0.001	2.09	0.61%
MgFeAl-1	0.824	0.189	0.002	2.15	1.15%
MgFeAl-5	0.821	0.177	0.010	2.20	5.37%
MgFeAl-10	0.801	0.170	0.020	2.11	10.44%
MgFeAl-25	0.739	0.129	0.044	2.13	25.32%
MgZnAl-0.5	0.814	0.190	0.005	2.15	0.57%
MgZnAl-1	0.804	0.193	0.009	2.10	1.15%
MgZnAl-5	0.762	0.189	0.043	2.12	5.32%
MgZnAl-10	0.710	0.181	0.081	2.18	10.26%
MgZnAl-25	0.571	0.176	0.189	2.16	24.90%
MgCoAl-0.5	0.615	0.146	0.002	2.12	0.86%
MgCoAl-1	0.799	0.192	0.006	2.12	2.07%
MgCoAl-5	0.744	0.201	0.025	2.04	9.22%
MgCoAl-10	0.697	0.190	0.044	2.18	15.85%
MgCoAl-25	0.568	0.172	0.107	2.59	36.19%

samples impurities of Si, Ca, S, Ni and Fe.† The absence of Na contamination confirmed sufficient washing of the LDHs after synthesis. None of the impurities listed were significant enough to greatly affect the $Co^{2+}/(Mg^{2+} + Co^{2+})$ ratio.

We believe that the increased presence of Co in the LDHs occurred as a result of the formation of a small, structurally similar and most likely amorphous Co side-species or a partially oxidised MgCoAl–LDH phase. This could be α-$Co(OH)_2$, which is structurally similar to the MgCoAl–LDH prepared and simulated by Rajamathi, Kamath and Seshadri (2002) in terms of its XRD pattern.[45] The formation of a partially oxidised MgCoAl–LDH phase of the form $MgCo^{2+}Co^{3+}Al$–CO_3^{2-}–LDH instead of its un-oxidised counterpart could also lie at the root of this problem. So too could the formation of numerous contaminant phases such as CoAl–LDH, $MgCo^{2+}Co^{3+}$–CO_3^{2-}–LDH similar to the NO_3^- intercalated form prepared by Xu and Zeng (2000),[46] or $Co^{2+}Co^{3+}$–CO_3^{2-}–LDH similar to that of Ma et al. (2008)[47] prepared with intercalated NO_3^-, be at the root of the problem.

Because of changes in oxidation state, bonding of the cations in the layer and interaction with the interlayer, these changes should be detectable using infrared spectroscopy (even for amorphous material). However, FTIR analysis (as discussed below) showed that it is unlikely that a large contaminant Co-containing phase was formed and the analysis could not give any clear indication of the phase formed. It could also be shown that the formation of an LDH species without Al is unlikely, considering the consistent presence of strong Al–OH stretching vibrations on the FTIR spectra discussed below.

FTIR spectra were obtained for all samples and are shown in Fig. 4 for the Co-substituted LDHs and in Fig. 5 for all other MgMAl–LDHs. The spectra obtained for the Fe-, Ni-, Cu- and Zn-substituted LDHs matched the MgAl–LDH well, while a lessening intensity of vibrational bands was observed for an increase in s in the MgCoAl–LDHs.

Typically, H-bonding stretching vibrations of the brucite-like layer OH-groups (M–OH bonds) in hydrotalcite are found between 3500 cm^{-1}–3600 cm^{-1}, but are dependent on the $M^{3+}/(M^{2+} + M^{3+})$ ratio.[2] A spectroscopic study of natural quintinite showed that three broad infrared bands exist between 3000 cm^{-1} and 4000 cm^{-1}, which correspond to the OH-stretching vibration (3388 cm^{-1}) and stretching vibrations of water units (3029 cm^{-1} and 3148 cm^{-1}).[48] Another study was more specific on the assignment of these three vibrations. At similar vibrational band positions to those discussed by Theiss et al. (2015), Kloprogge and Frost (1999) assigned the three bands to an M–OH stretching mode (3467 cm^{-1}), H-bonding of H_2O to interlayer anions (3297 cm^{-1}), and to CO_2–H_2O bridging (2972 cm^{-1}).[49] The same paper also found that the position of the bands is dependent on the TM used in the layer of the LDH.

The three bands mentioned above were observed in all prepared LDHs (albeit slightly shifted). The assignment of the peaks discussed by Theiss et al. (2015) fit the bands of this study better than those discussed by Kloprogge and Frost (1999) which can be explained by the use of a M^{2+}/M^{3+} ratio of 3 : 1 by Kloprogge and Frost (1999).[48,49] The band assigned to H-bonding of H_2O to interlayer anions (≈ 3148 cm^{-1}) was not as prominent for the LDHs prepared in this study compared to the intensity of the band in Theiss et al. (2015).[48]

In the mid-range of the FTIR spectra, a vibrational band at 1600 cm^{-1} that typically corresponds to water-bending[2] of molecules associated to the interlayer anion was observed at 1630 cm^{-1}.

On the lower end of the spectrum, Theiss et al. (2015) showed that vibrational bands at 776, 841, 866 and 949 cm^{-1} are linked to water librational modes.[48] Further, they assigned vibrational bands at 1350 cm^{-1} and 1407 cm^{-1} to CO_3^{2-} ν_3 antisymmetric stretching modes.[48] Other authors linked vibrations at 1012,
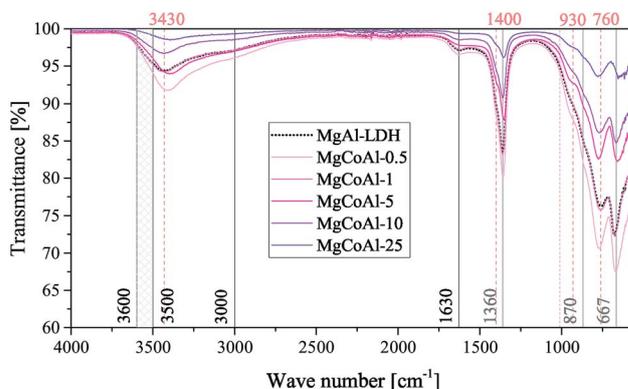
Fig. 4 FTIR results of the MgCoAl–LDH samples (s = 0.05%, 1%, 5%, 10% and 25%) with indication of the vibrations for the intercalated CO_3^{2-} species (grey), the typical vibrations for an LDH phase (black) and other important markers (apricot).
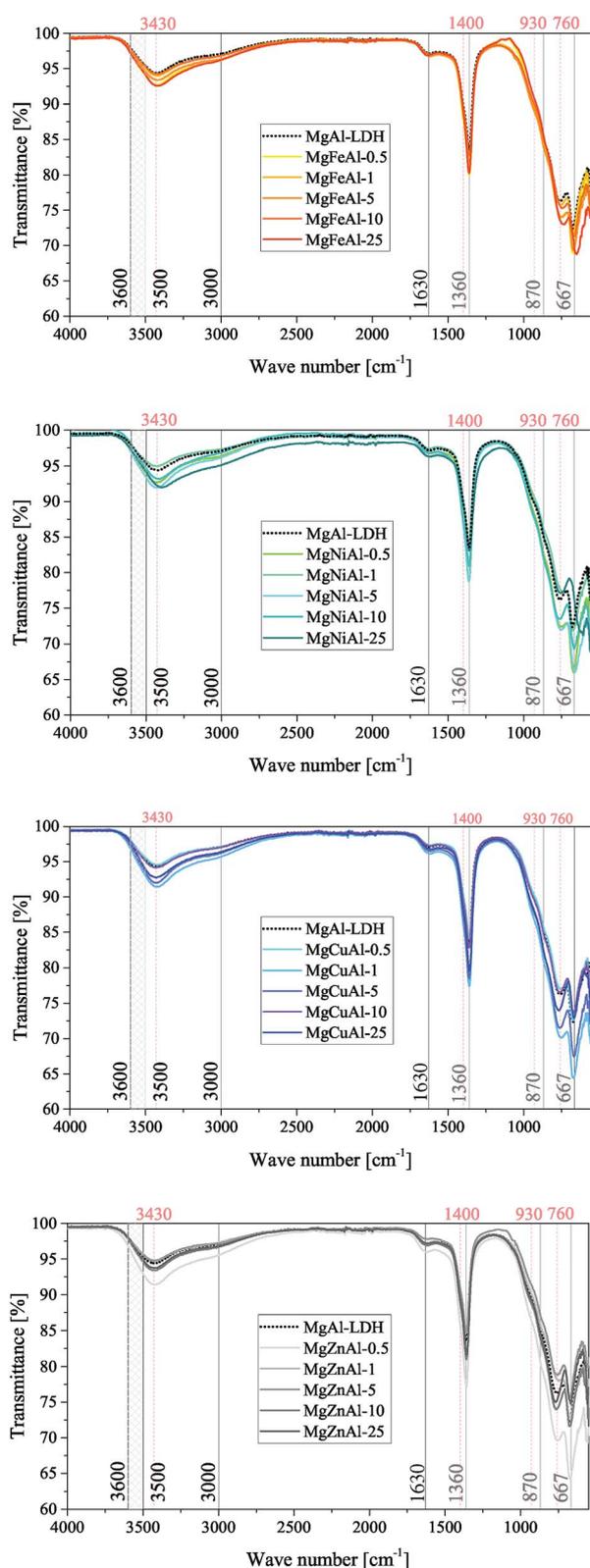
Fig. 5 FTIR results of the MgMAl–LDH samples (M = Fe, Ni, Cu and Zn) with vibrations for the intercalated CO_3^{2-} species (grey), the typical vibrations for an LDH phase (black) and other important markers (apricot) indicated.

870, 1365/1400 and 667 to the ν_1, ν_2, ν_3 and ν_4 vibrational modes of interlayer CO_3^{2-} respectively.[50] In addition to this, Kloprogge and Frost (1999) assigned a vibrations at 553, 597, 630, 759 and 939/1012 cm^{-1} to Al–OH translation, TM–O translation (Ni and Co), Mg–OH translation, Al–OH translation and a doublet Al–OH deformation respectively.

The spectra obtained for the MgMAl–LDHs exhibited vibrational bands at 1630, 1400, 1360, 930, 870, 760, 667 and ≈ 550 cm^{-1}. The presence of the ν_1 vibrational mode of interlayer CO_3^{2-} was not observed intensely. However, all other CO_3^{2-} vibrational modes described by Kloprogge et al. (2002) were clearly visible on the spectra.[50] Further, the CO_3^{2-} antisymmetric stretching modes at 1360 cm^{-1} and 1400 cm^{-1} were especially prominent. It was thus concluded that CO_3^{2-} was successfully intercalated into all LDHs. The remaining vibrations were assigned to Al–OH translation (≈ 550 cm^{-1} and ≈ 759 cm^{-1}), and Al–OH deformation (≈ 930 cm^{-1}). The Mg–OH translation band (≈ 630 cm^{-1}), was not very intense. Furthermore, slight shifts in the position of the ≈ 760 cm^{-1} vibration were observed and associated to an increasing amount of TM–O bonds and thus TM–O stretching vibrations.[51]

3.2 Morphology, surface area and platelet characteristics

A similar morphology was obtained for all LDHs. The micrographs in Fig. 6 show that the LDHs were synthesised as globular assemblies of nano-sized platelets (full size images are available in the ESI†). This morphology can frequently be observed for unaged, co-precipitated LDHs. However, the platelet size varied with the type and amount of TM-modification. Some samples showed the formation of tiny particles covering the globular platelet assemblies. This typically led to complications in filtering and increased difficulty in the post-processing of the LDHs in comparison to that of the globularly assembled LDHs. The morphology shown on the micrographs in Fig. 6 were also observed in other spots of the samples.

The following was observed as trends in the change of the morphology with an increase in TM substitution:

• MgFeAl–LDH: increase in platelet size and space between platelets with an increase in Fe-substitution.

• MgCoAl–LDH: first an increase in platelet size and space between the platelets, then a decrease in both.

• MgNiAl–LDH: first an increase in platelet size and space between the platelets, then a decrease in both.

• MgCuAl–LDH: slow increase in platelet size and space between the platelets.

• MgZnAl–LDH: increase in platelet size and increase in the space between the platelets.

Because the globular platelet assemblies achieved in this study were observed to be around 200 nm in size on the SEM micrographs, it was possible to calculate the crystallite sizes of the LDHs using the Scherrer equation

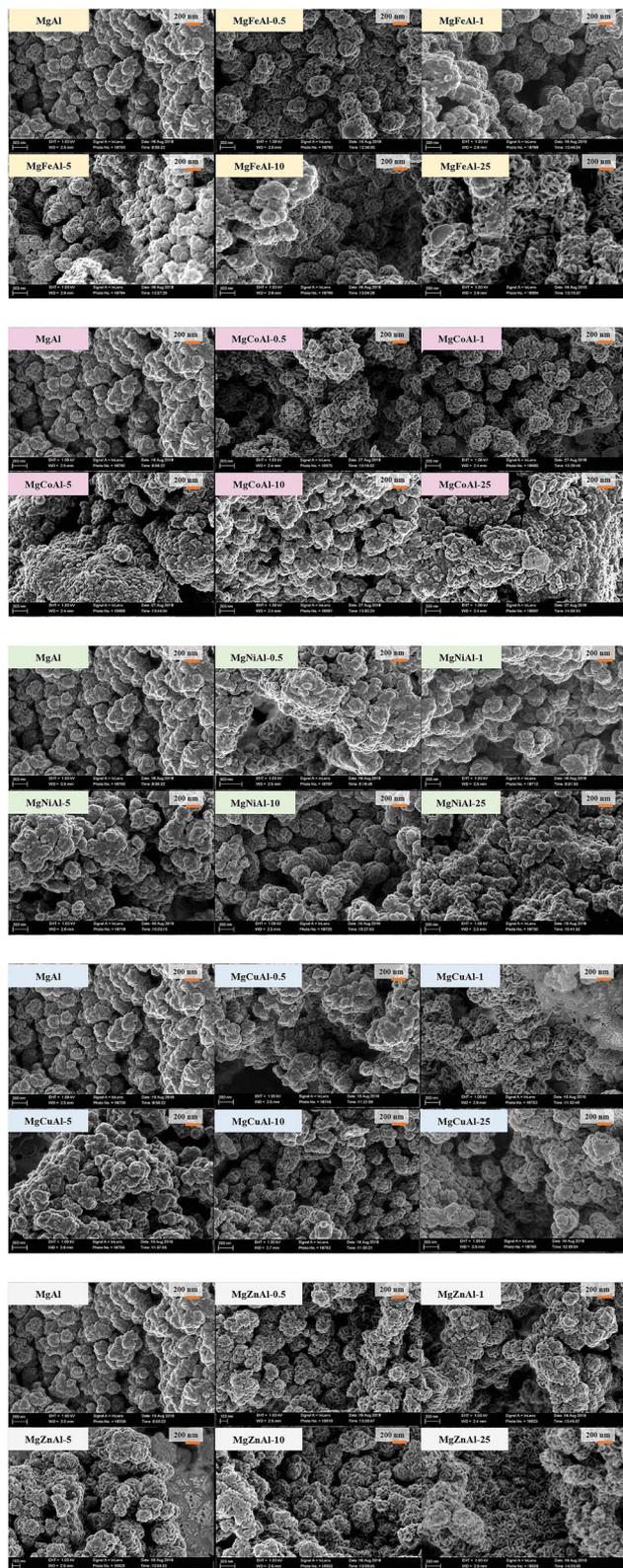$$\tau = \frac{K\lambda}{\beta \cos \theta}$$

Fig. 6 SEM micrographs (at 1 keV) of the TM-substituted MgMAl–LDHs synthesised.

β the full width at half maximum (FWHM) in radians and θ the Bragg angle in radians. In this study, K was used as 0.89 (ref. 53) and λ as 1.78897 Å for Co-Kα radiation.

Two crystallite dimensions were calculated: the crystallite size parallel to the LDH layers and the crystallite size perpendicular to the LDH layers. The FWHM and Bragg angle of reflection (003) was used for the perpendicular dimension and the FWHM and Bragg angle of reflection (110) was used for the parallel dimension. As the calculation of crystallite size typically requires subtraction of instrumental line broadening for the determination of an accurate FWHM, the crystallite sizes given here are only estimates.

All results are shown in Fig. 7. It was found that the observations from SEM regarding the changes in platelet size and the pore structure correlated extremely well to the crystallite sizes calculated. Overall, the smallest crystallites were obtained for the Ni-substituted LDHs ($s > 1\%$). Overall, the largest crystallites were obtained for MgFeAl-25. The crystallite sizes in direction parallel to the LDH layers were found not to follow a trend throughout the range of TM substitution. In terms of the crystallite thickness, however, a stable trend across the TM substitutions could be observed. The crystallite thickness increased with an increase in TM substitution (exception MgNiAl-10) and followed the general trend MgNiAl- $\approx$ MgZnAl- < MgCuAl- $\approx$ MgFeAl- < MgCoAl–LDH.

In conclusion, TM-modified LDHs prepared in this study showed more complex structures than reported by other authors. Parida *et al.* (2012) formed smaller but better separated platelets upon Fe-substitution.[14] Pu *et al.* (2013) formed particle agglomerates of 50–100 nm for Fe-substitution.[16] The particles were not as intertwined as in this study. Much larger, but similarly intertwined structures were prepared by Vulić *et al.* (2008) for Fe-substitution and size variations were observed with a change in the percentage of Fe-substitution.[23] Materials of similar morphology to those produced were prepared by Wang *et al.* (2011) (Ni-substituted),[15] Chagas *et al.* (2015) (Co-substituted),[30] and Zeng *et al.* (2016) (Cu-substituted).[54] Zheng *et al.* (2012) formed very-well-defined globular platelet assemblies (microspheres) but of much larger size (approx. 2 μm) for Zn-substituted LDHs.[19] Wang *et al.* (2013) and Wang *et al.* (2014) prepared similarly sized but well-separated platelets (Zn-substitution).[20,22] All materials mentioned in this comparison were post-treated (unlike those prepared in this study). However, different synthesis methods and conditions were used for most studies, especially in terms of the synthesis pH, post-treatment conditions and the concentration of the salt and base solutions used for co-precipitation. Because the synthesis conditions affect the morphology of the material greatly, obtaining differing morphologies between the different studies thus comes at no surprise. A thorough comparison between the data produced in this study to others could not be made, as the morphology of LDHs prepared, or the influence of metal composition on morphological changes, is frequently left unreported.

3.2.1 Sample treatment after synthesis and post-treatment. Mortar and pestle grinding is frequently employed to grind LDHs into powders after drying. PSA was used to investigate
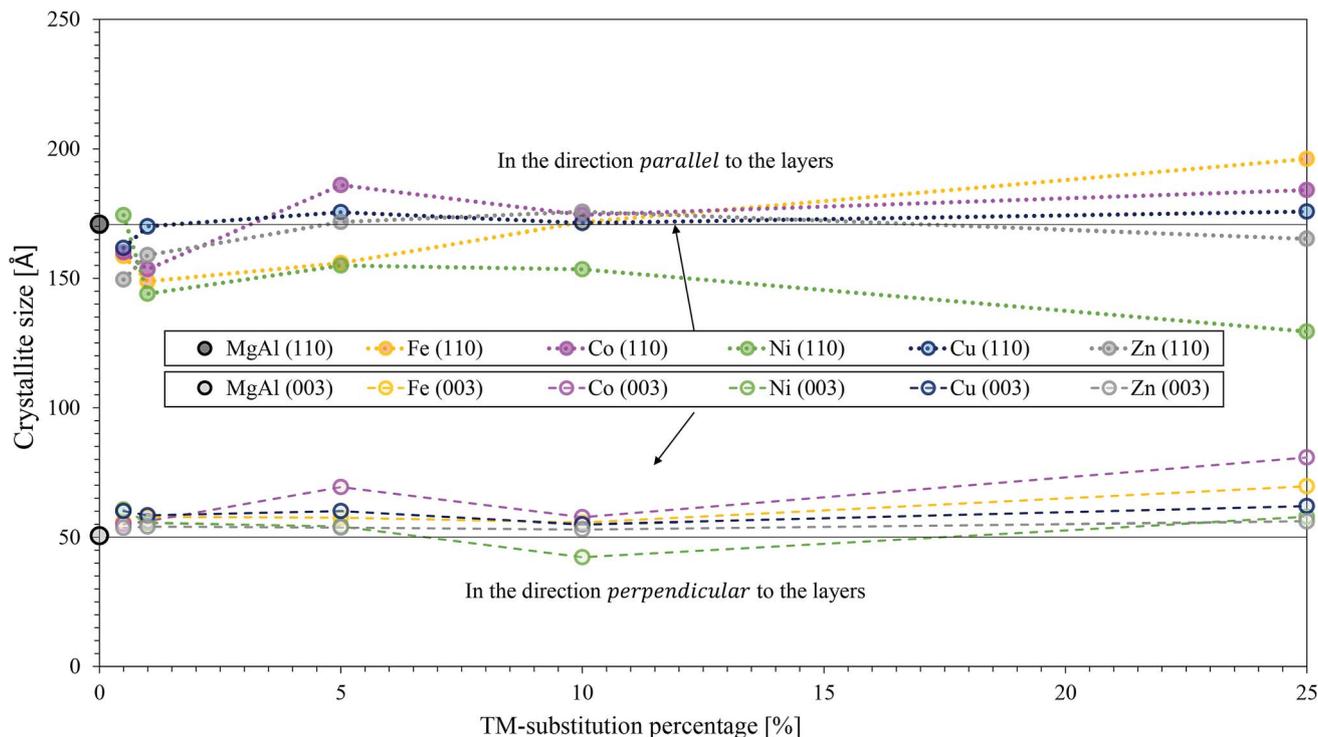
(valid for particles with a maximum size between 100 nm and 200 nm).[52] Here, τ is the crystallite size (units dependent on λ), K a shape factor, λ the X-ray wavelength used in XRD analysis,

Fig. 7 Comparison of crystallite sizes calculated from XRD data of the TM-substituted MgMAl–LDHs with M = Fe, Co, Ni, Cu and Zn. Crystallite sizes in the parallel and perpendicular direction are shown.

whether this method of sample preparation is sufficient for the production of samples that can be compared according to agglomerate size. The LDHs produced in this study formed globular platelet assemblies. It is also evident from SEM that these assemblies were agglomerated in larger structures. It thus comes to no surprise that PSA results showed that large agglomerates were present in the samples. As evidenced in Fig. 8, almost all samples were produced with a particle size distribution (PSD) peaking at 1 μm (small peak) and 10 μm (majority peak). However, some samples showed a more varied PSD (the Ni- and Co-substituted LDHs and MgCuAl-5).‡ The differences in agglomerate sizes of the LDHs could be ascribed to differences in the hardness of the samples' filtercakes after drying. The Ni- and Co-substituted LDHs dried as hard shards for substitutions exceeding 1%. The formation of hard shards made the grinding of the LDHs using a mortar and pestle difficult. All other LDHs formed very soft and crumbly filtercakes upon drying that were easy to grind with a mortar and pestle and broke down upon light application of pressure. In light of the PSA results shown, it is evident that mortar and pestle grinding is an insufficient method of preparation to obtain similarly size-distributed agglomerates across all TM substitutions. Mortar and pestle grinding is, however, an appropriate sample preparation method to produce similar PSDs for the series of Fe-, Cu- and Zn-substituted LDHs.

‡ It is believed that the multipeak PSA curve of MgCuAl-5 resulted through an error in PSA sample preparation.

3.3 Thermal stability

The TGA results of the TM-substituted LDHs are shown in the ESI.† Fig. 9 was constructed as a summary of the results for all samples and to show changes in the thermal degradation behaviour of the materials. TGA is a useful characterisation technique to determine the stability of LDHs in desired applications and is used to find optimum thermal post-treatment temperatures (calcination temperatures). The calcination of an LDH leads first to the loss of adsorbed surface species, then a loss of crystal water and volatile interlayer species, and, finally, conversion of the hydroxide layers to oxide layers (layered double oxide formation (LDO)).[1,2,55] To obtain this information, the LDH is typically heated from room temperature to the highest temperature of interest. For this study, 1000 °C was chosen – a temperature frequently applied to investigate the thermal degradation products of LDHs up to the irreversible formation of spinel- and mixed oxide phases.

Thermal decomposition of carbonate intercalated LDHs occurs as follows: at temperatures below and around 100 °C, adsorbed surface species are lost.[55] Then there typically exist two decomposition stages. The first stage is associated with the loss of interlayer water, the second with the dehydroxylation of the layers and loss of interlayer anions.[1] Hereby, the second stage can split into two distinct stages, the first being associated with the loss of OH⁻ bound to Al cations in the layer and the second to the loss of OH⁻ bound to Mg cations in the layer as well as the loss of interlayer carbonate anions. The loss of surface hydroxyl groups is associated with the conversion of the
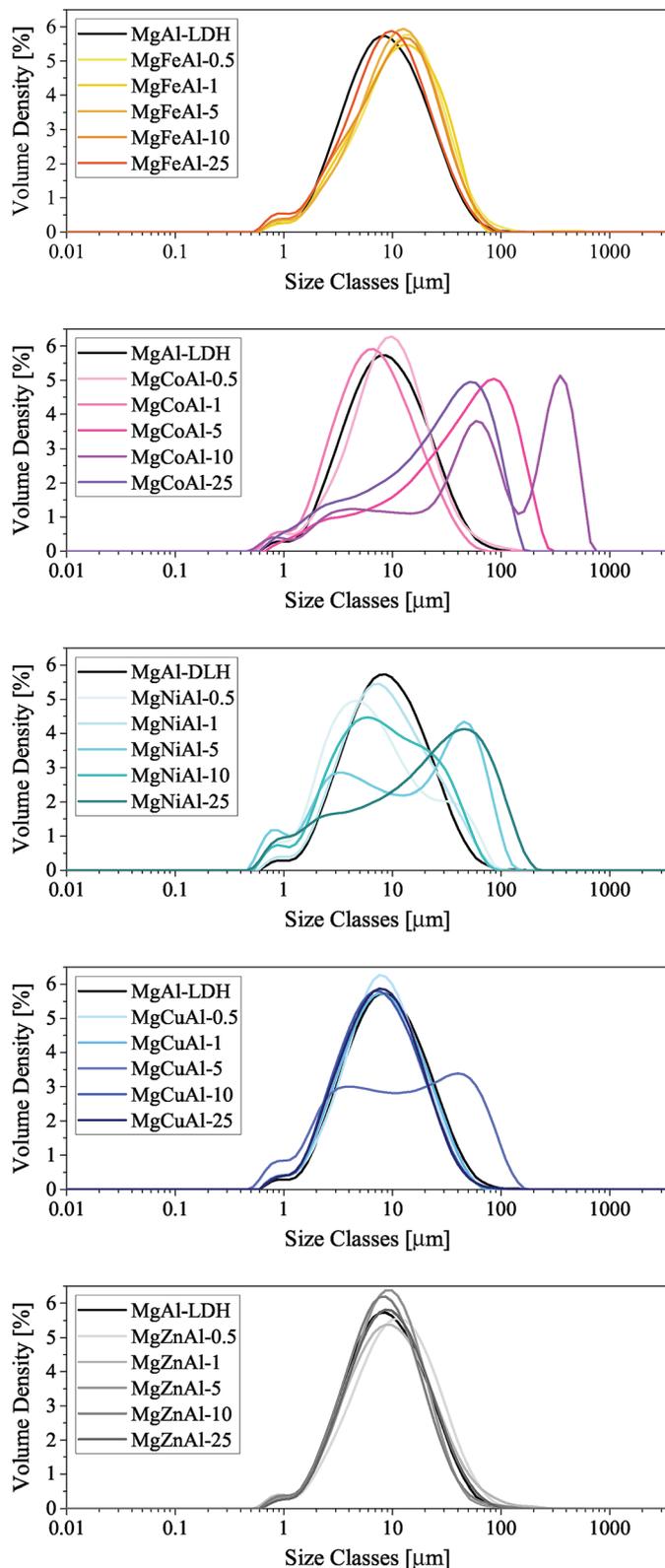
Fig. 8 PSA of the TM-substituted MgMAl–LDHs synthesised (NOTE: the x-axis label of these figures is not compiling correctly).

hydroxide- to oxide species. At this point, the LDH structure is retained as a layered double oxide species and rehydration is possible. Increasing the temperature further leads to the

formation of amorphous metal oxide and mixed metal oxide phases that ultimately convert into better crystallised (mixed) metal oxide and spinel phases. These products cannot be rehydrated to form LDH structures.[1,2]

3.3.1 Loss of adsorbed surface water and volatiles. Fig. 9 shows that the substitution of Fe, Ni, Cu and Zn led to a decrease in the maximum of the loss of adsorbed surface species with respect to MgAl–LDH, while the maximum of adsorbed surface species' loss remained mostly unaffected through the substitution of Co. MgCoAl-5, however, developed a double peak in this range. It is believed that this double peak resulted from an increased amount of adsorbed volatile surface species compared to the other samples. Rarely were the surface-species-loss peak and the interlayer-water-loss peak completely resolved. When they were, the mass loss of adsorbed surface species was close to 6% and never exceeded 9%.

3.3.2 Loss of interlayer water. TM substitution had a great effect on the retention of interlayer water. Substitution of Fe, Cu, Zn and Ni reduced the interlayer water retention with respect to MgAl–LDH, while Co-substitution increased the retention of interlayer water. Thereby, increasing substitution of Cu led to a decrease in retention of interlayer water, while increasing Ni-substitution led to an increase in the retention of interlayer water. The interlayer water retention remained approximately constant for Fe- and Zn-substitution. Finally, increasing Co-substitution led to an increase in interlayer water retention. When the surface-species-loss peak and the interlayer-water-loss peak were completely resolved, interlayer water loss was associated with a mass loss of $\approx 10\%$.

3.3.3 Dehydration mass loss. Since the mass-loss peak at ≈ 100 °C for adsorbed species and 150–200 °C for loss of interlayer water merged in most cases (the first typically being a shoulder), calculation of the true interlayer water content was not possible. However, some indications towards the water content could be found. Apart from the Ni-substituted LDHs, increases in TM-content led to decreases in overall mass loss between 100–200 °C (Fig. 10), indicating that a lower affinity for water absorption/adsorption must exist for higher TM substitutions. This matches with the layer d_{003} spacing, which decreased with an increase in TM substitution (for all but the Fe-substituted LDHs) as well as the a-parameter calculations (thickness of the layer). Thus, space between the layers was reduced and less water allowed to present.

3.3.4 Loss of Al-bound OH$^-$. TM substitution affected the position of the maximum loss of Al-bound OH$^-$. The increased substitution of Cu and Zn led to a decrease in the resistance to dehydroxylation of Al-bound OH$^-$. Changes in the substitution percentage of Fe did not affect the resistance to dehydroxylation, but Fe-substituted MgAl–LDH was less stable than plain MgAl–LDH. Substitution of Co increased the resistance to the dehydroxylation of Al-bound OH$^-$ compared to MgAl–LDH. A similar trend seemed to exist for Ni-substituted LDH. However, MgNiAl-25 only exhibited one decomposition peak (at ≈ 380 °C).

3.3.5 Decomposition of interlayer CO$_3^{2-}$ and loss of Mg-bound OH$^-$. The decomposition of the interlayer and loss of Mg-bound OH$^-$ was mostly unaffected by the amount of TM substituted. However, the type of TM substituted played a role.
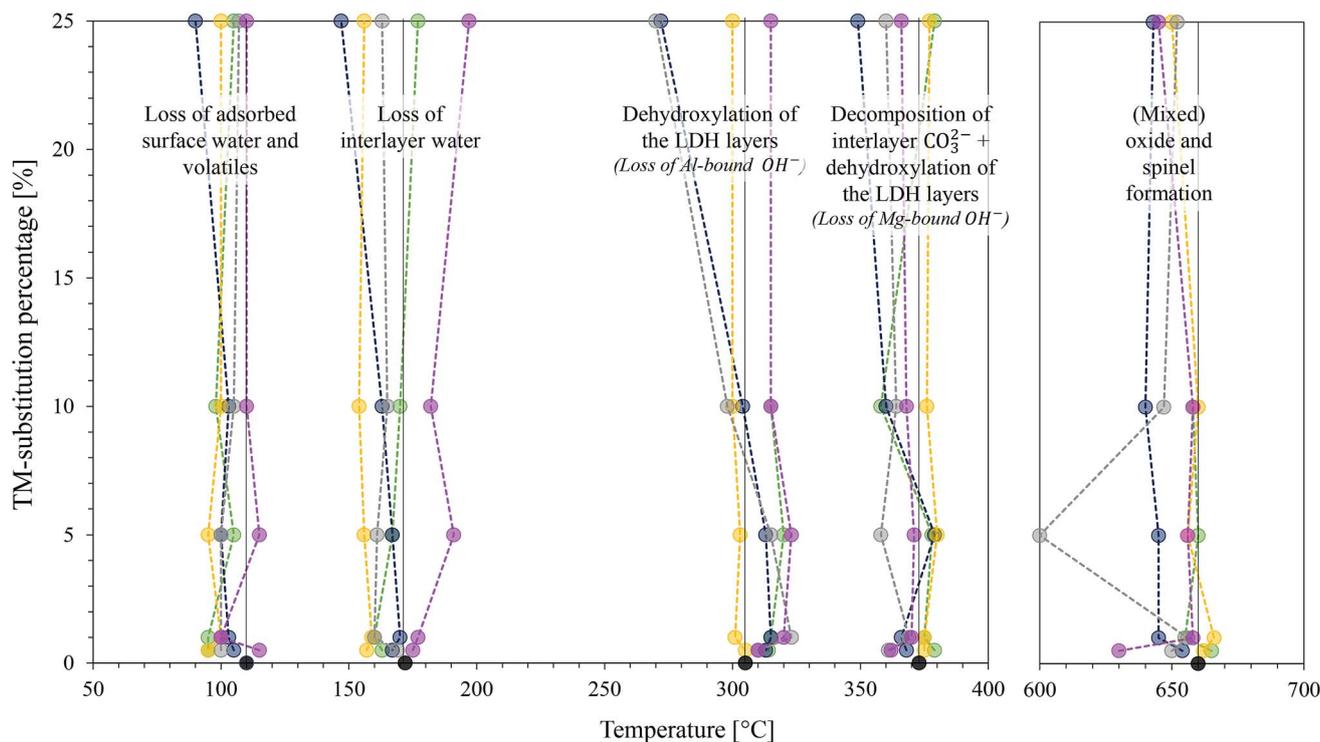
Fig. 9 Change in position of T_{max} of the derivative curve of the TGA profile with a change in TM-substitution percentage for all TM-substituted MgMAl–LDHs with M = Fe, Co, Ni, Cu and Zn. Decomposition stages are indicated. The usual colour spectrum applies: MgAl–LDH = black, Fe-subs. = yellow, Co-subs. = pink, Ni-subs. = green, Cu-subs. = blue and Zn-subs. = grey.

Overall, stability followed the trend MgCuAl- < MgZnAl- < MgCoAl- < MgAl- < MgNiAl- ≈ MgFeAl–LDH. Two outliers to this trend were observed: MgCuAl-5 and MgNiAl-10.

3.3.6 Dehydroxylation and decarbonation mass loss. The dehydroxylation and decarbonation peaks (≈300 °C to 400 °C) overlapped in some cases (MgNiAl-1, MgNiAl-5, MgNiAl-25,

MgFeAl-25, MgZnAl-5, and MgCoAl-25). All other LDHs exhibited well-separated peaks in the their derivative residue curves. The trends of total mass loss of these two steps are indicated in Fig. 10. Mass loss decreased with an increase in TM substitution for Cu-, Zn- and Co-substituted LDHs. The mass loss remained similar for the Fe-substituted LDHs and increased with an
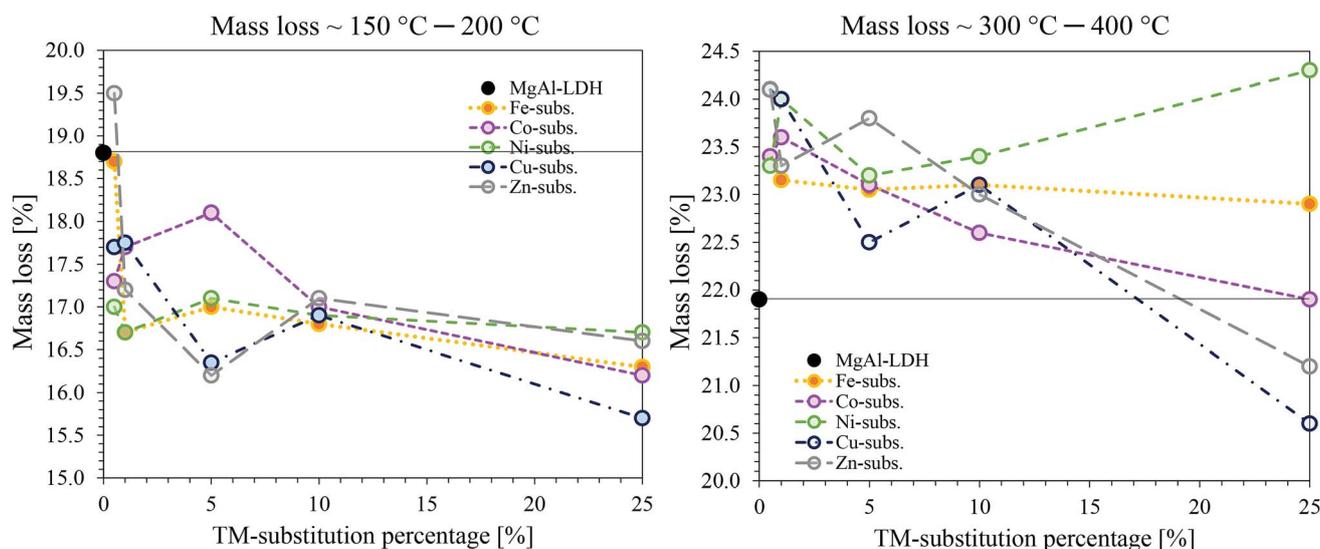

Fig. 10 Comparison of mass loss with the different TMs and TM substitutions. On the right: mass loss of the combined effect of adsorbed surface species and interlayer water loss (≈100 °C to 200 °C). On the left: Mass loss of the combined effect of dehydroxylation and decarbonation (≈300 °C to 400 °C).

increase in Ni-substitution. The combined mass loss for dehydroxylation and decarbonation exceeded that of plain MgAl–LDH in all cases but MgZnAl-25 and MgCuAl-25.

3.3.7 (Mixed) oxide and spinel formation. Small peaks in the derivative mass loss were observed at around 650 °C and correspond to exothermic effects of the crystallisation of spinel phases and mixed oxides.[56] A ≈ 4% mass loss was recorded for each sample.

A general trend could be observed at this stage, as the crystallisation effect was mostly unaffected by the TM-substitution percentage. The mixed oxides resulting from MgCuAl–LDH were found to be the least stable and underwent crystallisation to spinel phases at the lowest temperatures. This was followed very closely by MgZnAl–LDH, MgCoAl–LDH, MgFeAl–LDH and MgNiAl–LDH – the last to start crystallisation being MgAl–LDH.

MgNiAl-25 did not show any decomposition peak at $T >$ 400 °C. MgZnAl-5, MgCuAl-5, MgFeAl-25 and MgCuAl-25 had additional, very small mass loss peaks at 879 °C, 663 °C, 790 °C and 800 °C, respectively.

3.3.8 Residue at 950 °C. Overall, the percentage residue remaining did not deviate greatly (max deviation = 3.5%) from the MgAl–LDH standard. Further, analysis of the residue at 950 °C showed that an increasing TM substitution reliably led to an increase in percentage residue at 950 °C (Fig. 11). Compared against MgAl–LDH, only Co-substitution > 1%, Cu-, Zn-, and Ni-substitution > 5%, and Fe-substitution > 10% showed a greater percentage residue at 950 °C. Overall, the percentage residue at 950 °C followed the approximate trend MgFeAl- < MgNiAl < MgCuAl- < MgZnAl- < MgCoAl–LDH. The greatest effect of TM substitution was observed for Zn-substitution. Here, substitution of small (<5%) amounts of Zn significantly decreased the percentage residue retained, while high retention was observed for Zn-substitutions >5%.

Considering the molar masses of each of the metals, an increase in mass of residue is logical. Interesting was, however, that, although every substitution percentage should have led to an increase in residue-mass, this increase was only observed for substitutions ≥5%.

Negative deviation from the percentage residue of MgAl–LDH can indicate the presence of impurities. Based on the chemicals used for synthesis, possible impurities could be oxides, hydroxides, carbonates, chlorides or combinations thereof, of the metals present in the LDH. For the impurity to lose more mass than the LDH form, however, the metal would have to be coordinated to more volatile species than the LDH.

It has already been established through XRD analysis that all but four samples contained no crystalline impurity phases in amounts larger than 2%. Considering the TGA curves shown in the ESI† and the percentage residue remaining, it could be confirmed once more that impurities present are very small and amorphous. However, other than additional decomposition peaks at temperatures >600 °C for samples MgCuAl-5 (calumetite contamination confirmed with XRD), MgZnAl-5, MgFeAl-25 and MgCuAl-25, which could have been caused by impurities, no indication towards the nature of the impurity phases could be found through any of the characterisation techniques used in this study. Further, no comparable references could be found indicating decomposition temperatures of the impurities found through XRD analysis.

Finally, a note on the residue-mass retained of the TM-substituted LDHs. According to the difference in weight caused through substitution of higher weight cations into the LDH layers, the percentage residue remaining should have followed the trend Zn > Cu > Ni > Co > Fe. The observed trend, however, was Co > Zn > Cu > Ni > Fe. This matches with the XRF results showing a larger amount of Co present in the samples. Combined with the TGA results which showed no additional mass loss peaks and very similar results for all substitutions, this serves as an indication towards the formation of an LDH phase with increased Co-content or a structurally similar contaminant Co-phase, seeing that this would decompose in the regions of LDH decomposition and thus remain undetected.[57]

4 Conclusion

While the synthesis of LDHs and also quintinite is studied well, this study, for the first time, provides a comprehensive comparison between the materials obtained with commonly substituted TMs in the layer (Fe, Co, Ni, Cu and Zn) and varying substitutions (up to 25%).

The synthesis conditions used to prepare the LDHs led to the successful formation of all desired phases other than the Co-substituted LDHs. Considering all characterisation techniques used in this study, the LDHs could be synthesised with great purity and the desired composition (apart from Co-substituted LDHs). Further study of the Co-containing phase is advised to determine whether an impurity Co-phase or a partially oxidised $MgCo^{II+}Co^{III+}Al$–LDH phase was formed.

It was found that the amount and type of TM substituted influenced the a- and c-parameter, platelet dimensions, post-processing method required for comparable results, and thermal stability.

It was shown through calculation of crystallite sizes from XRD data using the Scherrer equation and corroborated with SEM observations, that the largest and thickest platelets overall were produced with Co-substitution, while the thinnest and smallest platelets were produced with Ni-substitution. While
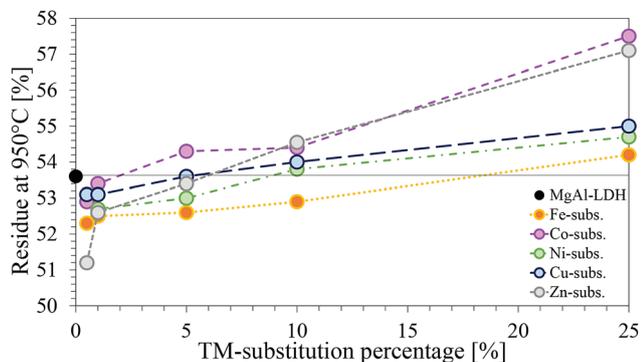
Fig. 11 Comparison of the residue remaining at 950 °C for each of the TM-substituted MgMAl–LDHs with M = Fe, Co Ni, Cu and Zn.

the platelet dimensions varied with TM substitution, the morphology of the materials remained remarkably similar in the form of nanostructured globular platelet assemblies.

Analysis of the TGA data showed that the interlayer water retention is weakest overall in Fe-substituted LDHs and strongest in Co-substituted LDHs. Decomposition of the layers (dehydroxylation and decarbonation) followed in a two-step process (first a loss of Al-bound OH^-, then a loss of Mg-bound OH^- and CO_3^{2-}). These two decomposition steps were dependent on the type and amount of TM substituted, and TM substitution influenced the amount of interlayer water present and the mass loss upon dehydroxylation and decarbonation.

Because the type and amount of TM substituted influenced the material properties with respect to size and thermal stability quite significantly, these differences should be taken into account when authors prepare materials to be compared against each other during application. Additionally, to obtain samples with comparable particle agglomerates, the frequently used mortar-and-pestle-grinding technique should be substituted with another sample preparation method.

Conflicts of interest

There are no conflicts to declare.

Acknowledgements

References

1 C. Forano, T. Hibino, F. Leroux and C. Taviot-Guého, *Handbook of Clay Science*, Elsevier, 2006, vol. 1, pp. 1021–1095.

2 F. Cavani, F. Trifirò and A. Vaccari, *Catal. Today*, 1991, **11**, 173–301.

3 X. Duan and D. G. Evans, *Layered Double Hydroxides*, Springer-Verlag Berlin Heidelberg, 2006, vol. 119, pp. 1–120.

4 J. J. Bravo-Suárez, E. A. Páez-Mozo and S. T. Oyama, *Quim. Nova*, 2004, **27**, 601–614.

5 S. J. Mills, A. G. Christy, J.-M. R. Génin, T. Kameda and F. Colombo, *Mineral. Mag.*, 2012, **76**, 1289–1336.

6 D. G. Evans and X. Duan, *Chem. Commun.*, 2006, 485–496.

7 Y. Zhao, X. Jia, G. I. Waterhouse, L.-Z. Wu, C.-H. Tung, D. O'Hare and T. Zhang, *Adv. Energy Mater.*, 2016, **6**, 1501974.

8 A. Gomes, D. Cocke, D. Tran and A. Baksi, in *Layered Double Hydroxides in Energy Research: Advantages and Challenges*, ed. A. Jha, C. Wang, N. R. Neelameggham, D. P. Guillen, L. Li, C. K. Belt, R. Kirchain, J. S. Spangenberger, F. Johnson, A. J. Gomes, A. Pandey and P. Hosemann, Springer International Publishing, Cham, 2016, pp. 309–316.

9 Y. Ohishi, T. Kawabata, T. Shishido, K. Takaki, Q. Zhang, Y. Wang, K. Nomura and K. Takehira, *Appl. Catal., A*, 2005, **288**, 220–231.

10 S. Tanasoi, G. Mitran, N. Tanchoux, T. Cacciaguerra, F. Fajula, I. Săndulescu, D. Tichit and I.-C. Marcu, *Appl. Catal., A*, 2011, **395**, 78–86.

11 L. Jin, B. Ma, S. Zhao, X. He, Y. Li, H. Hu and Z. Lei, *Int. J. Hydrogen Energy*, 2018, **43**, 2689–2698.

12 H. Düdder, K. Kähler, B. Krause, K. Mette, S. Kühl, M. Behrens, V. Scherer and M. Muhler, *Catal. Sci. Technol.*, 2014, **4**, 3317–3328.

13 M. del Arco, A. Fernández, C. Martín and V. Rives, *Appl. Clay Sci.*, 2009, **42**, 538–544.

14 K. Parida, M. Satpathy and L. Mohapatra, *J. Mater. Chem.*, 2012, **22**, 7350–7357.

15 Y.-B. Wang and J.-M. Jehng, *Chem. Eng. J.*, 2011, **175**, 548–554.

16 Y. B. Pu, J. R. Wang, H. Zheng, P. Cai and S. Y. Wu, *Research Efforts in Material Science and Mechanics Engineering*, 2013, pp. 21–25.

17 G. Ovejero, A. Rodríguez, A. Vallet, P. Gómez and J. García, *Water Sci. Technol.*, 2011, **63**, 2381–2387.

18 L. Obalová, K. Jirátová, F. Kovanda, M. Valášková, J. Balabánová and K. Pacultová, *J. Mol. Catal. A: Chem.*, 2006, **248**, 210–219.

19 Y.-M. Zheng, N. Li and W.-D. Zhang, *Colloids Surf., A*, 2012, **415**, 195–201.

20 G. Wang, M. Yang, Z. Li, K. Lin, Q. Jin, C. Xing, Z. Hu and D. Wang, *J. Nanopart. Res.*, 2013, **15**, 1882.

21 F. J. W. J. Labuschagné, D. M. Molefe, W. W. Focke, I. Van Der Westhuizen, H. C. Wright and M. D. Royeppen, *Polym. Degrad. Stab.*, 2015, **113**, 46–54.

22 G. Wang, D. Rao, K. Li and Y. Lin, *Ind. Eng. Chem. Res.*, 2014, **53**, 4165–4172.

23 T. Vulić, M. Hadnadjev and R. Marinković-Nedučin, *J. Microsc.*, 2008, **232**, 634–638.

24 T. Vulić, A. Reitzmann, J. Ranogajec and R. Marinković-Nedučin, *J. Therm. Anal. Calorim.*, 2012, **110**, 227–233.

25 A. C. Heredia, M. I. Oliva, U. Agú, C. I. Zandalazini, S. G. Marchetti, E. R. Herrero and M. E. Crivello, *J. Magn. Magn. Mater.*, 2013, **342**, 38–46.

26 S. Paikaray, J. Essilfie-Dughan and M. J. Hendry, *Geochim. Cosmochim. Acta*, 2018, **220**, 217–234.

27 O. D. Pavel, D. Tichit and I.-C. Marcu, *Appl. Clay Sci.*, 2012, **61**, 52–58.

28 S. Naseem, B. Gevers, R. Boldt, F. J. W. J. Labuschagné and A. Leuteritz, *RSC Adv.*, 2019, **9**, 3030–3040.

29 A. Tsyganok and A. Sayari, *J. Solid State Chem.*, 2006, **179**, 1830–1841.

30 L. Chagas, G. D. Carvalho, W. D. Carmo, R. S. Gil, S. Chiaro, A. L. ao, R. Diniz, L. D. Sena and C. Achete, *Mater. Res. Bull.*, 2015, **64**, 207–215.

31 T. Coelho, R. Micha, S. Arias, Y. E. Licea, L. A. Palacio and A. C. Faro, *Catal. Today*, 2015, **250**, 87–94.

32 K. Shekoohi, F. S. Hosseini, A. H. Haghighi and A. Sahrayian, *MethodsX*, 2017, **4**, 86–94.

33 J. Rivera, G. Fetter, Y. Jiménez, M. Xochipa and P. Bosch, *Appl. Catal., A*, 2007, **316**, 207–211.

34 U. Sikander, S. Sufian and M. A. Salam, *Procedia Eng.*, 2016, **148**, 261–267.

35 Y. Zhu, S. Zhang, B. Chen, Z. Zhang and C. Shi, *Catal. Today*, 2016, **264**, 163–170.

36 I.-C. Marcu, D. Tichit, F. Fajula and N. Tanchoux, *Catal. Today*, 2009, **147**, 231–238.

37 A.-E. Sakr, T. Zaki, O. Elgabry, M. Ebiad, S. El-Sabagh and M. Emara, *Appl. Clay Sci.*, 2018, **160**, 263–269.

38 S. Miyata, *Clays Clay Miner.*, 1980, **28**, 50–56.

39 F. Scholz and H. Kahlert, *ChemTexts*, 2015, **1**, 7.

40 V. Rives, *Layered Double Hydroxides: Present and Future*, Nova Science Publishers, 2001, pp. 39–92.

41 S. Britto, S. Joseph and P. Vishnu Kamath, *J. Chem. Sci.*, 2010, **122**, 751–756.

42 R. Dohrmann, K. B. Rüping, M. Kleber, K. Ufer and R. Jahn, *Clays Clay Miner.*, 2009, **57**, 686–694.

43 M. J. dos Reis, F. Silvério, J. Tronto and J. B. Valim, *J. Phys. Chem. Solids*, 2004, **65**, 487–492.

44 R. D. Shannon, *Acta Crystallogr. A*, 1976, **32**, 751–767.

45 M. Rajamathi, P. Kamath and R. Seshadri, *Mater. Res. Bull.*, 2000, **35**, 271–278.

46 Z. P. Xu and H. C. Zeng, *Chem. Mater.*, 2000, **12**, 2597–2603.

47 R. Ma, K. Takada, K. Fukuda, N. Iyi, Y. Bando and T. Sasaki, *Angew. Chem., Int. Ed.*, 2008, **47**, 86–89.

48 F. Theiss, A. López, R. L. Frost and R. Scholz, *Spectrochim. Acta, Part A*, 2015, **150**, 758–764.

49 J. Kloprogge and R. L. Frost, *J. Solid State Chem.*, 1999, **146**, 506–515.

50 J. T. Kloprogge, D. Wharton, L. Hickey and R. L. Frost, *J. Solid State Chem.*, 2002, **87**, 623–629.

51 X. Wang and L. Andrews, *J. Phys. Chem. A*, 2006, **110**, 10035–10045.

52 A. L. Patterson, *Phys. Rev.*, 1939, **56**, 978–982.

53 Y. Zhao, F. Li, R. Zhang, D. G. Evans and X. Duan, *Chem. Mater.*, 2002, **14**, 4286–4291.

54 Y. Zeng, T. Zhang, Y. Xu, T. Ye, R. Wang, Z. Yang, Z. Jia and S. Ju, *Appl. Clay Sci.*, 2016, **126**, 207–214.

55 V. Rives, *Mater. Chem. Phys.*, 2002, **75**, 19–25.

56 J. Valente, G. Rodriguez-Gattorno, M. Valle-Orta and E. Torres-Garcia, *Mater. Chem. Phys.*, 2012, **133**, 621–629.

57 Z. P. Xu and H. C. Zeng, *J. Mater. Chem.*, 1998, **8**, 2499–2506.